Chapter 5
Numerical Simulation on Rotating Detonation Engine: Effects of Higher-Order Scheme

Nobuyuki Tsuboi, Makoto Asahara, Takayuki Kojima, and A. Koichi Hayashi

Abstract The implementation and simulations of the robust weighted compact nonlinear scheme (RWCNS) for the two-dimensional rotating detonation engine are performed using the detailed chemistry model. The comparison of the MUSCL and the 5th-order RWCNS (WCNS5MN) indicates that the shock front and the contact surface for the WCNS5MN can be improved with the better resolution than those for the MUSCL and that both rotating velocities are approximately 97% of the CJ value. I_{sp} for the WCNS5MN is approximately 5 s larger than I_{sp} for the MUSCL because the mass flow rates for the WCNS5MN are 2–4% smaller than those for the MUSCL.

1 Introduction

Detonation is a strong explosion phenomenon that propagates at supersonic speed (e.g., a hydrogen/air detonation travels at supersonic). Detonation simulation requires to predict (i) a large discontinuous wavefront, such as a shock wave and a contact surface, and (ii) rapid chemical reaction near a combustion front. Because the detonation consists of strong explosion due to triple point collisions, the numerical scheme is required to be robust as well as numerical accuracy.

In the 1990s, the simulation of detonation was performed by the Harten-Yee total variation diminishing (TVD) scheme (Yee 1987) and the Godunov scheme

N. Tsuboi (✉)
Department of Mechanical and Control Engineering, Kyushu Institute of Technology, Kitakyushu, Fukuoka, Japan
e-mail: tsuboi@mech.kyutech.ac.jp

M. Asahara
Department of Mechanical Engineering, Gifu University, Yanagido, Gifu, Japan

T. Kojima
Chofu Aerospace Center, Japan Aerospace Exploration Agency, Chofu-shi, Tokyo, Japan

A. Koichi Hayashi
Department of Mechanical Engineering, Aoyama Gakuin University, Sagamihara, Kanagawa, Japan

J.-M. Li et al. (eds.), *Detonation Control for Propulsion*, Shock Wave and High Pressure Phenomena, https://doi.org/10.1007/978-3-319-68906-7_5

(Godunov 1959). In both cases, spatial accuracy reduces first-order near the discontinuities to add large numerical viscosity. In the 2000s, various numerical methods, such as the HLLE scheme (Einfeldt 1988), HLLC scheme (Batten et al. 1997), AUSMDV scheme (Wada et al. 1994), the weighted essentially non-oscillatory (WENO) scheme (Jiang et al. 1996), and the weighted compact nonlinear scheme (WCNS) (Deng and Zhang 2000) were applied to the simulation of detonation with the development of high-performance computers and computational methods.

Wintenberger and Shepherd (2003) simulated a pulse detonation engine (PDE) with the HLLE scheme. When we neglect the fine details of the phenomenon being simulated, a robust numerical method such as the HLLE scheme is effective. On the other hand, Togashi et al. (2009); Asahara et al. (2012), and Kurosaka and Tsuboi (2014) used the AUSMDV scheme for numerical simulation of detonation and showed the 2D and 3D wavefront structure in detail. Hu et al. (2005) and Henrick et al. (2006) showed the detonation front structure in further detail using a fifth-order WENO scheme. Schwer and Kailasanath (2013); Zhou and Wang (2012) simulated a rotating detonation engine (RDE) with the fifth-order WENO scheme.

Although WENO scheme is robust and superior scheme to simulate for strong shock waves with higher-order spatial accuracy, it is difficult to maintain a uniform freestream on an arbitrary grid system (Nonomura et al. 2010). WENO scheme is also probably not suitable for the simulation using a complex and crusterd grid(Nonomura et al. 2010). These problems do not arise in the detonation simulations because most of the detonation simulations with WENO scheme use a orthogonal grid system. Furthermore, large numerical dissipation affects the detonation structure because the WENO scheme uses the Lax-Friendrich scheme for numerical flux evaluation.

The authors simulated the multi-dimensional hydrogen-fueled detonations (Asahara et al. 2012; Tsuboi et al. 2002, 2007, 2009, 2008a, b, 2013a, b, 2017; Niibo et al. 2016; Eto et al. 2005; Tsuboi and Koichi Hayashi 2007; Eto et al. 2016) and hydrocarbon-fueled detonation (Araki et al. 2016) in a micro-scale size, which is the order of a millimeter and centimeter. However, three-dimensional simulations on an experimental scale are difficult because of a huge grid points and computational time. The authors pay their attention to a high-resolution scheme that can provide enough resolution for a simulation with a reduced number of grid points. The present study adopts the weighted compact nonlinear scheme (WCNS) (Deng and Zhang 2000; Nonomura et al. 2010; Zhang et al. 2008; Nonomura and Fujii 2009) in our in-house detonation simulation program, where the WCNS allows the AUSMDV scheme to be used. Some recent simulation results of the detonation using the fifth- and seventh-order WCNS scheme are reported by Iida et al. (2014) and Niibo et al. (2016). Nonomura et al. (2010) reported that the WCNS has three advantages: (i) the WCNS can select a wide variety of flux evaluations, (ii) the WCNS provides high resolution, and (iii) the WCNS can maintain a uniform flow on generalized curvilinear coordinates. Although the WCNS has such the advantages comparing with the WENO, the WCNS is sometimes failed to simulate the strong explosion just after the triple point collision in the detonation. The robust weighted compact nonlinear scheme (RWCNS) developed by Nonomura

and Fujii (2013), which improves robustness near a large discontinuity, succeeds to simulate the detonation with a detailed chemical reaction model (Niibo et al. 2016; Iida et al. 2014).

The present research discusses to improve the RWCNS for the reactive compressible fluid codes with multi-component gases and comparison of the two-dimensional numerical results between the MUSCL and the WCNS on the rotating detonation engine.

2 Governing Equations

Simulations of detonations are generally performed using the Euler equations, which include the equations for various chemical species associated with the relevant chemical reactions. As far as species diffusion speed, the effect of gas molecular diffusion on the momentum and energy equations is low because the propagation speed of detonation exceeds $3 < Ma$. Based on a consideration of the small effect of the boundary layer behind the detonation front, we consider the possibility that the effect of viscosity on detonation is small. On the other hand, it is easy to compare between numerical schemes in the inviscid flow because the amount of the numerical viscosity, which depend on the choice of the numerical scheme, affects the resolution in the flowfields. For the above reasons, this study applies the compressible Euler equations to the modeling of shock waves and detonation.

The governing equations (the compressible Euler equations) consist of the mass conservation law of gases, the momentum conservation law, the energy conservation law, and the conservation law of each species. In the case of the two-dimensional Cartesian coordinate system, the compressible Euler equations are

$$\frac{\partial \mathbf{Q}}{\partial t}+\frac{\partial \mathbf{E}}{\partial x}+\frac{\partial \mathbf{F}}{\partial y}=\mathbf{S}, \tag{5.1}$$

$$\mathbf{Q}=\begin{pmatrix}\rho\\ \rho u\\ \rho v\\ e\\ \rho_1\\ \vdots\\ \rho_N\end{pmatrix},\mathbf{E}=\begin{pmatrix}\rho u\\ \rho u^2+p\\ \rho uv\\ (e+p)u\\ \rho_1 u\\ \vdots\\ \rho_N u\end{pmatrix},\mathbf{F}=\begin{pmatrix}\rho v\\ \rho uv\\ \rho v^2+p\\ (e+p)v\\ \rho_1 v\\ \vdots\\ \rho_N v\end{pmatrix},\mathbf{S}=\begin{pmatrix}0\\ 0\\ 0\\ 0\\ \dot{\omega}_1\\ \vdots\\ \dot{\omega}_N\end{pmatrix}, \tag{5.2}$$

where ρ is the density in kg/m^3, u and v are the velocity in the x and y directions in m/s, e is the total energy per specific volume in J/m^3, i is the index of the chemical species ($i = 1, 2, \cdots, N$), N is the total number of species, ρ_i is the density of the ith species in kg/m^3, p is the pressure in Pa, and ω_i is the production rate of the ith

species by the chemical reaction in kg/(m^3 · s), respectively. The total energy per specific volume, e, is defined as

$$e = \sum_{i=1}^{N} \rho_i h_i - p + \frac{1}{2}\rho\left(u^2 + v^2\right), \tag{5.3}$$

where h_i is the specific enthalpy of the ith species in J/kg.

An additional equation is needed to combine with Eq. (5.1) to form a closed system. We assume a thermally perfect gas and the equation of state of which is given by

$$p = \rho \bar{R} T = \sum_{i=1}^{N} \rho_i R_i T = \sum_{i=1}^{N} \rho_i \frac{R}{W_i} T, \tag{5.4}$$

where $\bar{R}$ is the gas mixture constant in J/(kg · K), R is the universal gas constant in J/(kmol · K), T is the temperature in K, and R_i is the gas constant for the ith species in J/(kg · K), which is given by

$$R_i = \frac{R}{W_i} \tag{5.5}$$

where W_i is the molecular weight in kg/kmol. The detonation simulation is calculated using the system of equations formed by the compressible Euler equations (Eq. 5.1) and the equation of state (Eq. 5.4).

The specific enthalpy of the ith species in Eq. (5.6) is given by a fifth-order polynomial function of temperature,

$$\frac{h_i}{R_i T} = a_{1i} + a_{2i} T + a_{3i} T^2 + a_{4i} T^3 + a_{5i} T^4 + \frac{a_{6i}}{T} \tag{5.6}$$

In the same way, the specific heat at constant pressure of the ith species, $C_{p,i}$, is defined by a fourth-order polynomial function of the temperature,

$$\frac{C_{p,i}}{R_i} = a_{1i} + a_{2i} T + a_{3i} T^2 + a_{4i} T^3 + a_{5i} T^4 \tag{5.7}$$

where a_{1i}, a_{2i}, a_{3i}, a_{4i}, a_{5i}, and a_{6i} are the coefficients calculated from the data in the JANAF tables (Stull and Prophet 1971). The specific heat ratio γ is written as

$$\gamma = \frac{\bar{C}_p}{\bar{C}_v} = \frac{1}{1 - \bar{R}\bar{C}_p}. \tag{5.8}$$

The gas mixture constant, $\bar{R}$, the gas mixture specific heat at constant pressure, $\bar{C}_p$, and the gas mixture specific enthalpy, $\bar{h}_i$, are defined as

$$\bar{R} = \sum_{i=1}^{N} Y_i R_i, \bar{C}_p = \sum_{i=1}^{N} Y_i C_{p,i}, \bar{h} = \sum_{i=1}^{N} Y_i h_i, \tag{5.9}$$

where

$$Y_i = \frac{\rho_i}{\rho}. \tag{5.10}$$

The speed of sound, c, is calculated from the following frozen speed of sound:

$$c^2 = p_\rho + \sum_{i=1}^{N} Y_i p_{\rho_i} + p_e \left(H - u^2 - v^2 \right), \tag{5.11}$$

where

$$p_\rho = \frac{\partial p}{\partial \rho}, p_{\rho_i} = \frac{\partial p}{\partial \rho_i}, p_e = \frac{\partial p}{\partial e}, H = \bar{h} + \frac{1}{2}\left(u^2 + v^2 \right). \tag{5.12}$$

H in Eq. (5.12) is the total enthalpy.

3 Chemical Kinetic Model

One- and Two-Step Reaction Model

The most simplified reaction model used for detonation calculation is one-step reaction model. This model describes the combustion with a heat release Q behind a shock wave by using the reaction progress parameter Z which varies continuously from 1 to 0. On the other hand, the two-step model was developed by Korobeinikov et al. (1972) having a structure of two sequences; the induction reaction period and heat release period. This model applies for the conservation equation using an induction reaction progress parameter α and recombination reaction progress parameter β instead of the conservation equation of species, where α and β are unity at the initial state before reaction happens. The recombination reaction starts after the induction reaction is over and α becomes zero. K_j, n_j, l_j, m_i, E_i (i = 1, 2 and j = 1,2,3), and Q are the constants which are obtained empirically. The following Eqs. (5.13) and (5.14) are used instead of the species conservation equation in Eq. (5.1).

$$\frac{\partial \rho\alpha}{\partial t}+\frac{\partial \rho\alpha u}{\partial x}+\frac{\partial \rho\alpha v}{\partial y}=\rho\omega_{\alpha} \tag{5.13}$$

$$\frac{\partial \rho\beta}{\partial t}+\frac{\partial \rho\beta u}{\partial x}+\frac{\partial \rho\beta v}{\partial y}=\rho\omega_{\beta} \tag{5.14}$$

$$\omega_{\alpha}\equiv\frac{d\alpha}{dt}=-\frac{1}{\tau_{ind}}=-k_1 p^{n_1}\rho^{l_1}\exp\left(-\frac{E_1}{RT}\right) \tag{5.15}$$

$$\omega_{\beta}\equiv\frac{d\beta}{dt}=\begin{cases}-k_2 p^{n_2}\rho^{l_2}\beta^{m_2}\exp\left(-\dfrac{E_2}{RT}\right)+ \\ k_3 p^{n_3}\rho^{l_3}\left(1-\beta\right)^{m_3}\exp\left(-\dfrac{E_2}{RT}\right), \alpha\le 0 \\ 0, \alpha>0\end{cases} \tag{5.16}$$

It is not necessary, in the case that the mixture is assumed as a simple ideal gas, to add a change in the energy conservation equations if the heat release Q is put in the enthalpy and energy equations as follows:

$$h=c_v T+\beta Q, e=\rho h-p+\frac{1}{2}\rho\left(u^2+v^2\right) \tag{5.17}$$

where the chemical reaction is not stiff using such two-step mechanism and the equations are integrated explicitly.

One- and Two-Step Reaction Model

In the case using a detailed chemical reaction mechanism for the small mechanism of hydrogen/oxygen reaction, the intermediate species such as H, O, OH, HO_2, and H_2O_2 are necessary for the calculation besides H_2, O_2, and H_2O. In this case, the chemical species are eight and their elementary reactions are about twenty. Two-dimensional calculation provides triple calculation time comparing with a non-reacting flow case because of five governing equations and nine more species equations. Since the equation system is stiff with a detailed reaction model, its production term is integrated implicitly and since heat capacities of species are a function of temperature, the calculation time becomes totally at least more than three times comparing with that without the reaction term.

As far as detonation propagating through a hydrogen/air mixture, it is necessary to analyze it using a reaction mechanism with nitrogen, but mostly nitrogen is considered as a third body because the nitrogen related reactions are rather slow comparing with the oxyhydrogen reactions. As for the hydrogen/air reaction model used

in detonation calculation, Oran et al. (1979) proposed eight species and 43 elementary reactions in 1979. They also proposed eight species and 24 elementary reactions (1982) in 1982. Shepherd (1986) also proposed in 1986. He studied the relationship between calculated reaction zone length and measured cell size. This reaction model has a set of 23 reactions and 11 species (H_2 , O_2 , O , H , OH, H_2O, HO_2 , H_2O_2 , N_2 , CO_2 , CO).

Recent several detailed chemical kinetic mechanisms of hydrogen combustion have been developed and are being updated by many researchers (Petersen and Hanson 1999; Mueller et al. 1999; Li et al. 2004; O'Conaire et al. 2004; Konnov 2008: Davis et al. 2005; Saxena and Williams 2006; Shimzu et al. 2011). These models have been validated using a wide range of measurements and were generally found to agree with experimental data, including ignition delay times with shock tubes, reaction behavior in flow reactors, and laminar flame speeds. Rate constants and third-body efficiencies for many elementary reactions seem to be evident in hydrogen/oxygen systems. However, determining some rate constants characterized by high sensitivity at high pressures has remained a challenge.

Although predictions of those models agree quite well with each other and with the experimental data of ignition delay times and flame speeds at pressures lower than 10 atm, substantial differences are observed between recent experimental data of high-pressure mass burning rates and model predictions, as well as among the model predictions themselves. Different pressure dependencies of mass burning rates above 10 atm in different kinetic models result from using different rate constants in these models for HO_2 reactions, especially for H + HO_2 and OH + HO_2 reactions. The rate constants for the reaction H + HO_2 involving different product channels were found to be very important for the prediction of high-pressure combustion characteristics. In order to obtain better performance of the model prediction for the high-pressure combustion of H_2, UT-JAXA model (Shimzu et al. 2011) adopts more precise values of the rate constants for the following reactions:H + OH + M = H_2O + M, O + OH + M = HO_2 + M, channel-specific rate constants for H + HO_2, and the temperature dependence of the OH + HO_2 = H_2O + O_2 reaction.

The production rate of each species relevant to the two-body reaction, ω_i, in Eq. (5.1) is given by

$$\dot{\omega}_i = W_i \sum_{k=1}^{K} \left(\nu_{ik}^{''} - \nu_{ik}^{'}\right) \left\{ k_{f,k} \prod_{i=1}^{N} \left(c_{\chi_i,k}\right)^{\nu_{ik}^{'}} - k_{b,k} \prod_{i=1}^{N} \left(c_{\chi_i,k}\right)^{\nu_{ik}^{''}} \right\}, \tag{5.18}$$

where χ_i is the chemical symbol for the ith species (e.g., hydrogen: $\chi = H_2$), $\nu_i^{'}$ is the stoichiometric coefficient of the reactants for the ith species, $\nu_{ik}^{''}$ is the stoichiometric coefficient of the products for the ith species, the subscript k is the index of the elementary reactions ($k = 1, 2, \ldots, K$), K is the total number of elementary reactions, $k_{f,k}$ is the forward specific reaction-rate constant of the kth elementary reaction, and $k_{b,k}$ is the backward specific reaction-rate constant for the kth elementary reaction,

respectively. The forward specific reaction-rate constant of the kth elementary reaction is given by the modified Arrhenius rate law:

$$k_{f,k} = A_k T^{n_k} \exp\left(-\frac{E_{a,k}}{RT}\right), \tag{5.19}$$

where A_k is the frequency factor of the kth elementary reaction, n_k is the exponent that determines the power-law relationship between the temperature and the forward specific reaction-rate constant, and $E_{a,k}$ is the activation energy per unit mass of the kth elementary reaction in cal/mol. Values for A_k, n_k, and $E_{a,k}$ are provided by the detailed reaction model by UT-JAXA model (Shimzu et al. 2011). $k_{b,k}$, the backward reaction rate constant of kth reaction which is related with the forward reaction rate constant is given as follows

$$k_{b,k} = k_{f,k} / K_{c_k}, \tag{5.20}$$

where K_{c_k} is the concentration equilibrium constant of kth reaction. When K_{p_k} is the pressure equilibrium constant,

$$K_{c_k} = K_{p_k} \left(\frac{p_{atm}}{RT}\right)^{\sum_{i=1}^{N}\left(\nu_{ik}^{''}-\nu_{ik}^{'}\right)}, \tag{5.21}$$

where $p_{atm} = 1(atm)$ and R is the universal gas constant with an unit of T/P_{atm}. K_{p_k} is shown in the next Eq. (5.22) which is related with enthalpy and standard entropy.

$$K_{p_k} = \exp\left[\sum_{i=1}^{N}\left\{\left(\nu_{ik}^{''}-\nu_{ik}^{'}\right)\frac{s_i^0}{R_i}\right\} - \sum_{i=1}^{N}\left\{\left(\nu_{ik}^{''}-\nu_{ik}^{'}\right)\frac{h_i}{R_i T}\right\}\right]. \tag{5.22}$$

The frequency of three-body reactions is promoted by the fact that the third body (that is, the third molecule) absorbs energy from the other two molecules. By multiplying the production rate of the two-body reaction, given in Eq. (5.18), by the mole concentration of the third body, C_M, the production rate of the three-body reaction is obtained to be

$$\dot{\omega}_i = W_i C_M \sum_{k=1}^{K}\left(\nu_{ik}^{''}-\nu_{ik}^{'}\right)\left\{k_{f,k}\prod_{i=1}^{N}\left(c_{\chi_i,k}\right)^{\nu_{ik}^{'}} - k_{b,k}\prod_{i=1}^{N}\left(c_{\chi_i,k}\right)^{\nu_{ik}^{''}}\right\}. \tag{5.23}$$

The mole concentration of the third body, C_M, is given by

$$C_M = \sum_{i=1}^{N}\left(\alpha_{ik} c_{\chi_i}\right), \tag{5.24}$$

where α_{ik} is the collision coefficient of the third body for the ith species. The values of these collision coefficients are indicated by the UT-JAXA detailed reaction model (Shimzu et al. 2011).

4 Numerical Methods

In the detonation simulation in this study, an explicit method is used to solve the convective term and a point implicit method is applied to solve the source term of the chemical reaction, respectively. For the time integration, a third-order total validation diminishing Runge-Kutta scheme (TVDRK) (Gottlieb and Shu 1998) is used. The convective term is calculated by the AUSMDV scheme using flux evaluation with conservative variables that are interpolated at high orders by the WCNS. In the source term, a Crank-Nicholson type point implicit method is used. The inversion of Jacobian matrix in the source term is carried out by Gauss-Jordan elimination (Odlyzko 1985). The details are shown as follows.

Time Integration

In order to solve the governing equations of reactive flow in Eq. (5.1), a splitting technique into two parts is applied to treat for the difference of chemical kinetic time scale and fluid dynamic time scale. The partial equation for the fluid dynamic is solved by the TVDRK and the ordinary differential equation for the chemical kinetics is solved by the point implicit method. The detail of the procedure is shown as follows:

$$\mathbf{Q}^{n+1} = L_{PDE}^{\Delta t} L_{ODE}^{\Delta t} \mathbf{Q}^{n}, \tag{5.25}$$

$$L_{PDE}^{\Delta t} : \frac{\partial \mathbf{Q}}{\partial t} + \frac{\partial \mathbf{E}}{\partial x} + \frac{\partial \mathbf{F}}{\partial y} = 0, \tag{5.26}$$

$$L_{ODE}^{\Delta t} : \frac{d\mathbf{Q}}{dt} = \mathbf{S}. \tag{5.27}$$

Because of the superposition of the solution obtained from each differential operator, Eq. (5.25) corresponds to solving the following equations:

$$\mathbf{Q}^{*} = \mathbf{Q}^{n} + \Delta t L_{PDE}^{\Delta t}\left(\mathbf{Q}^{n}\right) \tag{5.28}$$

$$\mathbf{Q}^{n+1} = \mathbf{Q}^{*} + \Delta t L_{ODE}^{\Delta t}\left(\mathbf{Q}^{*}\right)$$

Here, Eq. (5.26), which serves as the partial differential equation for fluids, is applied to a following three-stage third-order TVDRK:

$$\begin{aligned}\mathbf{Q}^{(1)} &= \mathbf{Q}^n + \Delta t L\left(\mathbf{Q}^n\right)\\ \mathbf{Q}^{(2)} &= \frac{3}{4}\mathbf{Q}^n + \frac{1}{4}\mathbf{Q}^{(1)} + \frac{1}{4}\Delta t L\left(\mathbf{Q}^{(1)}\right)\\ \mathbf{Q}^{*} &= \frac{1}{3}\mathbf{Q}^n + \frac{2}{3}\mathbf{Q}^{(2)} + \frac{2}{3}\Delta t L\left(\mathbf{Q}^{(2)}\right)\end{aligned} \tag{5.29}$$

These equations yield conservative variables that represent the solution of the differential equation for the fluid at $t + \Delta t$.

Spatial Discretization Method

The method of evaluating the spatial differential term ($\partial\mathbf{E}/\partial x$) in Eq. (5.26) is shown below along the computational procedure in the simulation code. In this study, the WCNS is implemented to provide nonlinear interpolation to improve the accuracy of the simulation, and a robust linear difference scheme suggested by Nonomura and Fujii (2013) is used. The present schemes are summarized in Table. 5.1.

Nonlinear Interpolation

Interpolation is a method of constructing new data points within the range of a discrete set of known data points. In this case, the conservative variables Q_j on the grid point j are used to calculate $Q^L_{j+1/2}$ and $Q^R_{j+1/2}$, i.e. on the left and right sides of the cell interface in Fig. 5.1.

The WCNS is the nonlinear interpolation method used to determine the value at the computational cell interface, which is needed to evaluate the numerical flux. The WCNS uses the value at the node point. A previous study of the WCNS (Nonomura et al. 2012) indicated that the interpolation by using primitive variables is robust against the oscillation in the vicinity of the interference, where gas species vary drastically, and that the interpolation by conservative variables is robust to the

Table 5.1 Simulation methods for present scheme

	Nonlinear interpolation	Flux evaluation	Linear Interpolation
MUSCL	2nd-order MUSCL	AUSMDV	2nd-order central difference with minmod limiter[49]
WCNS5MN6	5th-order RWCNS	AUSMDV	Eq. (5.47) with 6th-order coefs

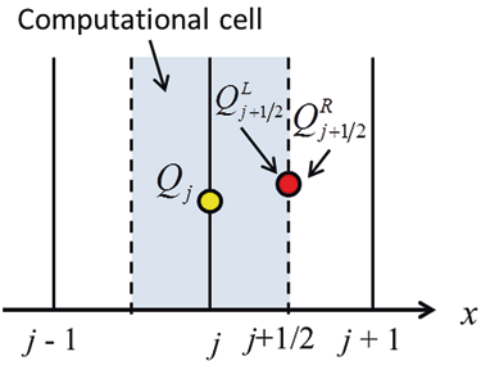

Fig. 5.1 Interpolation in the computational cell with $2r$-1 stencil points

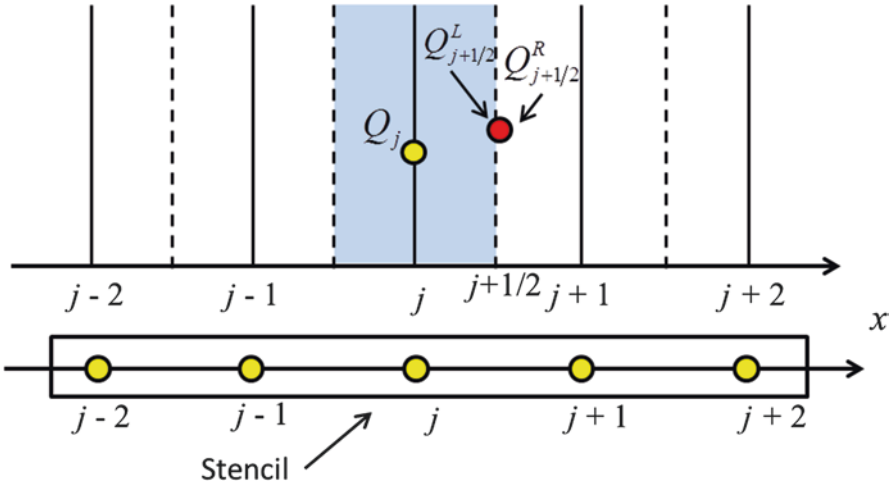

Fig. 5.2 Stencil at the point j for $r = 3$ (5th-order interpolation)

oscillation around shock waves. The detonation front structure is constructed by the complicated shock waves so that the interpolation by conservative variables is suitable for the simulation of detonation. From this perspective, the conservative variables are used in the interpolation of the WCNS.

In order to calculate the conservative variables at the computational cell interface, stencils $S_{j+1/2}$ of $2r-1$ points are used to construct the conservative variables $Q^L_{j+1/2}$ and $Q^R_{j+1/2}$ with a $(2r-1)$th-order interpolation:

$$S_{j+12} = \left\{ x_{j-r+1}, , , , \cdots, , , , , x_j, , , , \cdots, , , , , x_{j+r-1} \right\}. \tag{5.30}$$

For example, if $r = 3$, five points $(j-2\,, j-1\,, j\,, j+1\,, j+2)$ are required and a 5th-order interpolation is performed in Fig. 5.2.

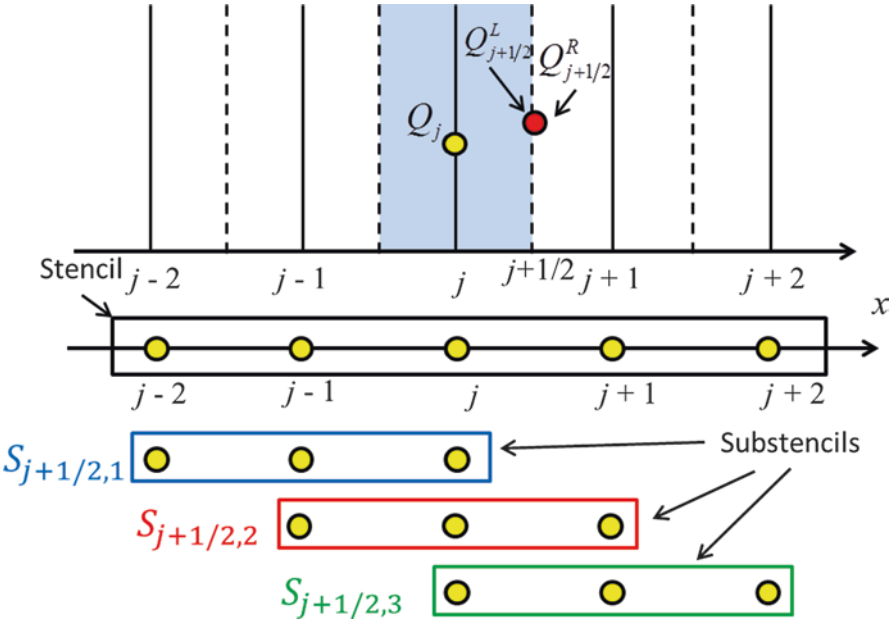

Fig. 5.3 Substencils for interpolation at the point j for $r = 3$ (5th-order interpolation)

The first step is to transform the conservative variables $\mathbf{Q}$ in the stencil to the characteristic variables $q_{j,\ m}$ by multiplying the left eigenvector, yielding the expression

$$q_{j,m} = \mathbf{l}_{j,m}\mathbf{Q}_j, \tag{5.31}$$

where the mth left eigenvectors of the Jacobian matrix $\partial\mathbf{E}/\partial\mathbf{Q}$ are $\mathbf{l}_{j\ ,\ m}$ and the mth characteristic variables are $q_{j,\ m}$. The second step is to construct polynomials consisting of (r substencils. The r substencils are composed of r cell centers in Fig. 5.3. The kth substencil $S_{j\ +\ 1/2\ ,\ k}(k = 1,\cdots,\ r)$ is written as

$$S_{j+12,k} = \left\{x_{j+k-r},,,,,\cdots,,,,,x_j,,,,,\cdots,,,,,x_{j+k-1}\right\}. \tag{5.32}$$

Then, points of each substencil are combined to calculate an $(2r - 1)$th-order interpolation in Fig. 5.4.

The characteristic variables in the kth polynomials $q^L_{j+1/2,k,m}$ are computed as

$$q^{(n)}_{j,k,m} = \sum_{l=1}^{r} c_{n,k,l} \cdot q_{j+k-r+l-1,m}. \tag{5.33}$$

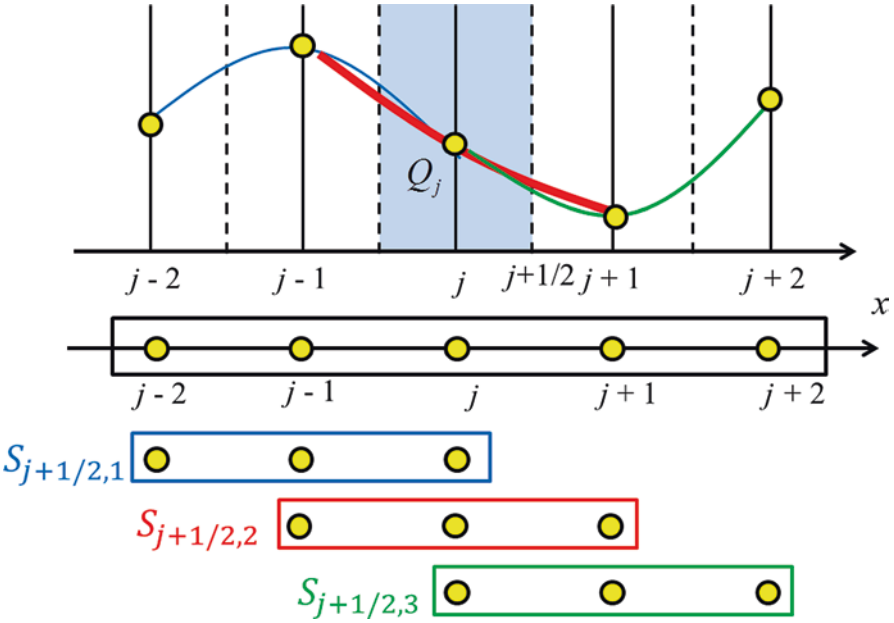

Fig. 5.4 5th-order interpolation by combination of each substencil ($r = 3$)

Here, the details of coefficients $c_{n,\,k,\,l}$ are shown in Nonomura and Fujii [5.33]. For example, the approximation of the 1st derivative of the mth characteristic variable at the 1st substencil ($n = 1$, $r = 3$) is expressed as:

$$q^{(1)}_{j,1,m} = c_{1,1,1} \cdot q_{j-2,m} + c_{1,1,2} \cdot q_{j-1,m} + c_{1,1,3} \cdot q_{j,m}. \tag{5.34}$$

By reproducing the same calculation for other kth substencils and other nth derivatives with their own c coefficients, we can obtain a full data set to calculate the weighted characteristic variables for each substencil at the cell interface as follows:

$$q^{L}_{j+1/2,k,m} = q_{j,m} + \sum_{n=1}^{r-1} \left(\frac{1}{n!} \right) \left(\frac{\Delta x}{2} \right)^{n} q^{(n)}_{j,k,m}. \tag{5.35}$$

This calculation is based on the Taylor expansion method which represents a function as an infinite sum of terms that are calculated from the values of the function's derivatives at a single point. In the case of $r = 3$(5th-order), the mth weighted characteristic variable for the k substencils can be written as:

$$q^{L}_{j+1/2,k,m} = q_{j,m} + \frac{\Delta x}{2} q^{(1)}_{j,k,m} + \frac{1}{2} \frac{\Delta x^2}{4} q^{(2)}_{j,k,m}. \tag{5.36}$$

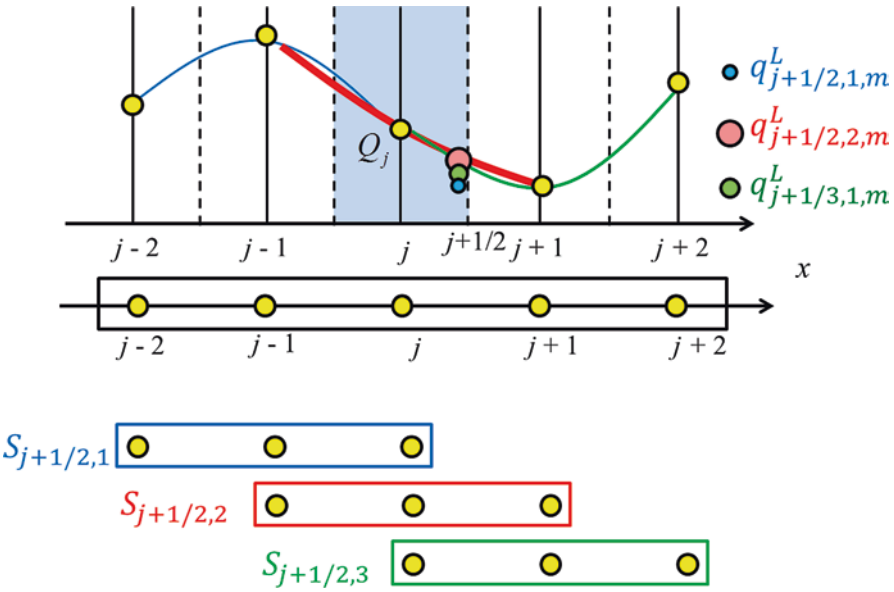

Fig. 5.5 Weighted characteristic variable at the left edge of the cell from each substencil ($r = 3$, 5th-order interpolation)

If we consider the 1st substencil, the above equation becomes:

$$q^L_{j+1/2,k,m} = q_{j,m} + \frac{\Delta x}{2}\left[c_{1,1,1}\cdot q_{j-2,m} + c_{1,1,2}\cdot q_{j-1,m} + c_{1,1,3}\cdot q_{j,m}\right] + \frac{\Delta x^2}{8}\left[c_{2,1,1}\cdot q_{j-2,m} + c_{2,1,2}\cdot q_{j-1,m} + c_{2,1,3}\cdot q_{j,m}\right]. \tag{5.37}$$

The idea is that a weight is assigned to each of the k substencils. It determines the contribution of the substencil to the final approximation of the cell-edge value $q_{j+1/2,m}$ in Fig. 5.5. The obtained variables in Eq. (5.37) are rth order cell-edge interpolated values.

The third step is to combine these characteristic variables $q^L_{j+1/2,k,m}$ together with a new final weight coefficient w_k to calculate a final $(2r-1)$th-order accurate interpolation value $q^L_{j+1/2,m}$ at the cell interface. This combination is done as follows:

$$q^L_{j+1/2,m} = \sum_{k=1}^{r} w_{j+1/2,k,m}\cdot q^L_{j+1/2,k,m}, \tag{5.38}$$

where

$$w_{j+1/2,k,m} = \frac{\alpha_{j+1/2,k,m}}{\sum_{l=1}^{r}\alpha_{j+1/2,l,m}}, \tag{5.39}$$

$$\alpha_{j+1/2,k,m} = \frac{C_k}{\left(IS_{j+1/2,k,m}\right)^2 + \varepsilon}, \tag{5.40}$$

$$IS_{j+1/2,k,m} = \sum_{l=1}^{r} \left(q^{(n)}_{j+1/2,k,m}\right)^2. \tag{5.41}$$

In Eq. (5.40), ϵ is a very small value $\epsilon = 1 \times 10^{-6}$, which avoids the division by zero. The meaning of Eqs. (5.39), (5.40) and (5.41) is that if a polynomial of the form of Eq. (5.35) becomes smooth, i.e. in continuous regions, $w_{j+1/2,k,m}$ approaches to C_k. On the other hand, near discontinuities, $w_{j+1/2,k,m}$ decreases to prevent from numerical oscillations. This may result in a slight loss of accuracy but the stability of the calculation is improved. $w_{j+1/2,k,m}$ has to satisfy the following equation:

$$\sum_{k=1}^{r} w_{j+1/2,k,m} = 1. \tag{5.42}$$

Finally, multiplying Eq. (5.38) by the right eigenvectors of the matrix $\partial\mathbf{E}/\partial\mathbf{Q}$, $\mathbf{r}_{j,m}$, the conservative variables, $\mathbf{Q}_{j+1/2}$, can be calculated:

$$\mathbf{Q}^L_{j+1/2} = \sum_m q^L_{j+1/2,m} \cdot \mathbf{r}_{j,m}. \tag{5.43}$$

When $\mathbf{Q}^L_{j+1/2}$ is calculated, $\mathbf{Q}^R_{j+1/2}$ can be obtained symmetrically with a similar way.

Flux Evaluation

By using the conservative variables at the computational cell interface $\mathbf{Q}^L_{j+1/2}$ and $\mathrm{Q}^R_{j+1/2}$ in Eq. (5.43), the numerical flux at the computational cell interface, $\mathbf{E}_{j+1/2}$, is calculated. The equation used for the flux evaluation in the AUSMDV scheme is

$$\tilde{\mathbf{E}}_{j+12} = \frac{1}{2}\left\{(\rho u)_{12}\left(\Psi_R + \Psi_L\right) - \left|(\rho u)_{12}\right|\left(\Psi_R + \Psi_L\right)\right\} + p_{12}\mathbf{I}_2, \tag{5.44}$$

where

$$\Phi = \begin{pmatrix} \rho \\ \rho u \\ \rho v \\ \rho h \\ \rho_1 \\ \vdots \\ \rho_N \end{pmatrix}, \psi = \begin{pmatrix} 1 \\ u \\ v \\ h \\ Y_1 \\ \vdots \\ Y_N \end{pmatrix}, \mathbf{I}_2 = \begin{pmatrix} 0 \\ 1 \\ 0 \\ 0 \\ 0 \\ \vdots \\ 0 \end{pmatrix}. \tag{5.45}$$

The methods used to evaluate the pressure term, mass flux term, and momentum flux term are described in the original paper (Wada and Liou 1994).

Linear Difference

An approximation of flux derivative $\left(\frac{\partial \mathbf{E}}{\partial x}\right)_j$ is evaluated from $\tilde{\mathbf{E}}_{j+1/2}$. A general form of the explicit midpoint-to-node differencing (MD) scheme in Fig. 5.6 is written as follows:

$$\left(\frac{\partial \mathbf{E}}{\partial x}\right)_j = \frac{1}{\Delta x}\sum_{k=0}^{r-1} a_k \left(\tilde{\mathbf{E}}_{j+k+1/2} - \tilde{\mathbf{E}}_{j+k-1/2}\right). \tag{5.46}$$

On the other hand, the robust scheme for the RWCNS that Nonomura and Fujii (2013) improved as a midpoint-and-node-to-node difference (MND) in Fig. 5.7 is given by

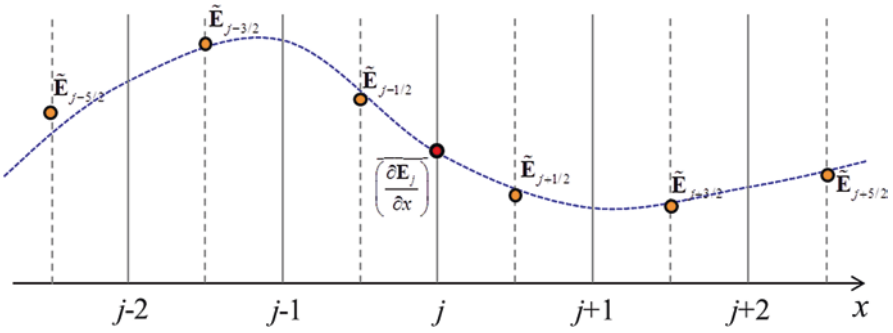

Fig. 5.6 Midpoint-to-node linear differentiation

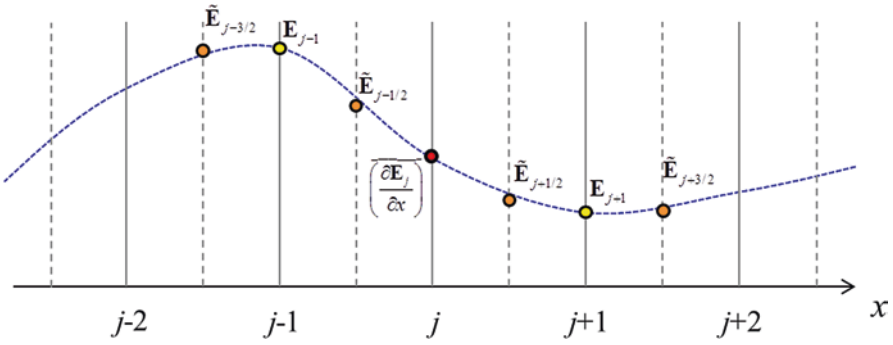

Fig. 5.7 Midpoint and node-to-node linear differentiation

$$\left(\frac{\partial \mathbf{E}}{\partial x}\right)_j = \frac{1}{\Delta x}\sum_{k=1}^{r} b_k\left(\tilde{\mathbf{E}}_{j+k/2} - \tilde{\mathbf{E}}_{j-k/2}\right), \tag{5.47}$$

$$\tilde{\mathbf{E}}_{j\pm k/2} = \begin{cases} \tilde{\mathbf{E}}_{j\pm k/2}\left(k = 2n-1\right), \\ \mathbf{E}_{j\pm k/2}\left(k = 2n\right) \end{cases}, \tag{5.48}$$

where the true flux at the node point is $\mathbf{E}_{j\pm k/2}$. The coefficients of a_k and b_k are shown in the original article by Nonomura and Fujii (2013). When Eq. (5.48) is substituted into Eq. (5.47), the true flux is interpolated into the numerical viscosity term.

This scheme in Eq. (5.47) prevents the negative numerical viscosity around the shock wave and improves stability more than the original scheme in Eq. (5.46). Thus, the difference between the WCNS and the RWCNS is the linear interpolation. The present research uses the nonlinear interpolation as 5th-order RWCNS and linear interpolation as Eq. (5.47) with 6th-order coefficients.

5 Simulation Conditions

The simulation conditions and grid system used in this study are presented in Table 5.2. The computational regions for the x- and y- directions are 3 mm × 6 mm.

The ambient conditions behind the exit are pressure p_e of 0.01 MPa and temperature of 300 K. The reason to use low ambient pressure is the comparison of I_{sp} between the present simulation and H_2/O_2 conventional rocket engine without nozzle under vacuum condition. The simulation conditions in the stagnation chamber are pressure p_0 of 2–6 MPa and temperature of 300 K. The micro-nozzle area ratios of the throat to nozzle exit at the injection port, A^*/A, are 0.02. The stoichiometric H_2/O_2 gas mixture is supplied through the micro-nozzles. The numerical setup of the present simulation and boundary conditions are shown in Fig. 5.8.The numerical

Table 5.2 Simulation conditions and computational grids (constant resolution)

p_0, MPa	L, mm (imax)	H, mm (jmax)	Δx , Δy, μm[a]1	A^a/A
2	3.0 (1201)	6.0 (2401)	2.5	0.2
3	3.0 (1451)	6.0 (2901)	2.07	0.2
4	3.0 (1543)	6.0 (3087)	1.95	0.2
5	3.0 (1593)	6.0 (3187)	1.89	0.2

[a]1: approximately five grid points in H_2 half reaction length

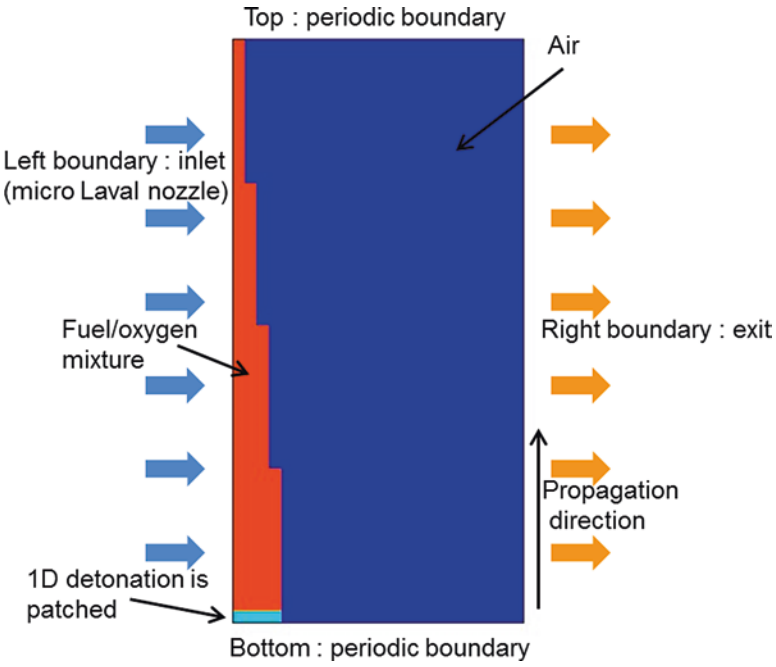

Fig. 5.8 Numerical setup and boundary conditions

result of the one-dimensional detonation is used for the ignition in the two-dimensional simulation. As the stagnation pressure is lower than 2 MPa, the rotating detonation becomes failure. Although the successful of the detonation ignition will depend on the stoichiometric ratio and stagnation temperature in the injection gas, the present simulations does not estimate the effect of them yet.

There are two boundary condition systems for the mixture injection: the supersonic and subsonic inlets. The supersonic inlet condition is used for most of the simulations because the inlet nozzles for premixed gas typically have a choked condition at the exits of small nozzles. However, a supersonic inlet condition exists in many real cases because of the high pressure in the combustion chamber. The subsonic inlet condition is discussed by Zhdan et al. (2007). The present calculations are performed based on the following four conditions:

1. The pressure is extrapolated, and velocity is set to zero when the inlet pressure is higher than the manifold pressure. This case means that the gas injection is impossible.
2. The pressure is extrapolated when the pressure just before the inlet is lower than the manifold pressure and higher than the pressure just behind the inlet. In this case, there is no choking at the throat with a subsonic gas injection.
3. The pressure is extrapolated when the inlet pressure is higher than the supersonic condition and lower than the subsonic condition. In this case, a normal shock wave is generated in the nozzle with the subsonic injection.

4. The pressure achieves a supersonic value and the premixed gas is accelerated due to isentropic expansion with supersonic injection when the inlet pressure is higher than the supersonic condition.

The outlet boundary conditions are given at the exit of the RDE by two patterns, but the flow cannot go backwards from the downstream to the upstream:

1. The exit pressure of the RDE is set to the ambient pressure when the exhaust gas speed is subsonic.
2. The exit pressure of the RDE is extrapolated from the values in the combustion chamber when the exhaust gas speed is supersonic.

The effects of the grid resolution on the MUSCL are discussed by Tsuboi et al. (2013, 2015, 2017). As the grid resolution increases in 2D and 3D RDE simulations, a cellular structure appears near the detonation head. However, the effects of the grid resolution on the I_{sp} is approximately a few seconds.

6 Results and Discussions

Basic Flow Structure

The comparison of the density gradient between the MUSCL and the WCNS5MN is presented in Fig. 5.9. The injection conditions are $A^*/A = 0.2$ and $p_0 = 2.0$ MPa. For both cases, some triple points appear near the detonation front. The rotating

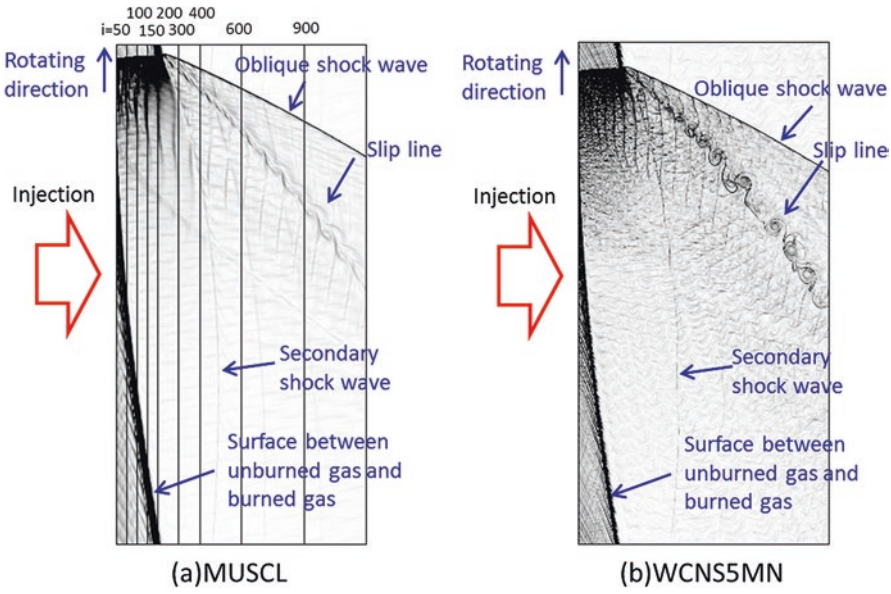

Fig. 5.9 Instantaneous density gradient contours and flow structure for $p_0 = 2$ MPa

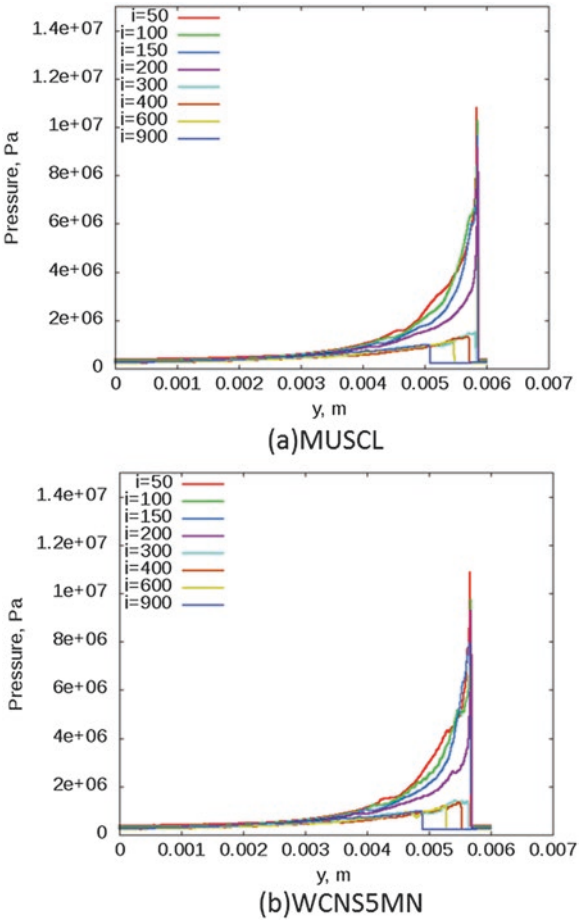

Fig. 5.10 Instantaneous pressure profile along y-directions in Fig. 5.9 for p_0= 2 MPa

detonation head produces some shock waves and a slip line. The WCNS5MN can resolve the slip line with small vortices better than the MUSCL.

Figure 5.10 plots the pressure along the lines near the injection, as shown in Fig. 5.9. The pressure behind the rotating detonation along lines $i = 50 - 900$ decreases because of the strong expansion in the unconfined region. Both pressure profiles show similar feature.

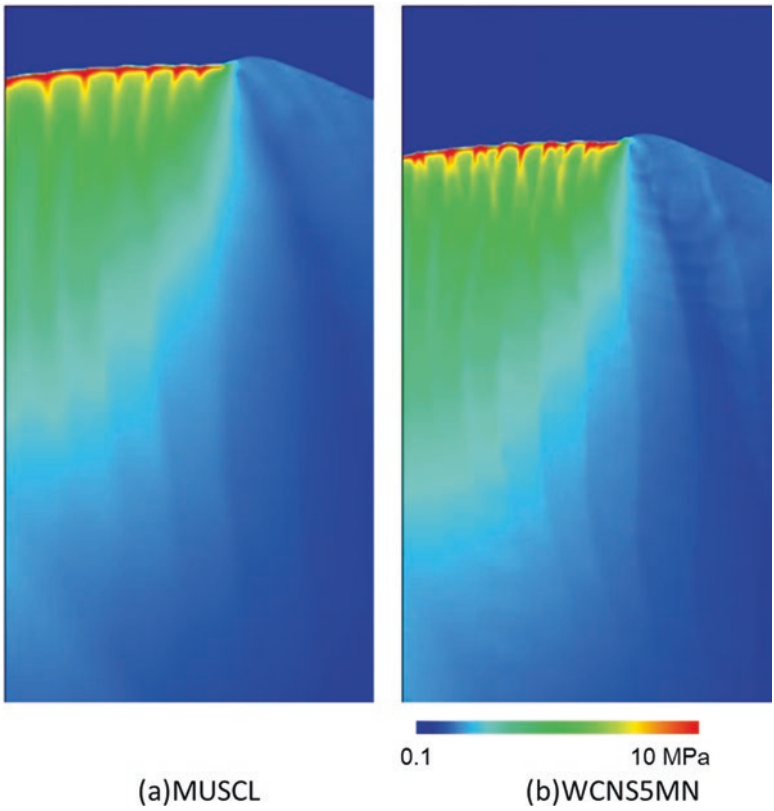

Fig. 5.11 Instantaneous pressure contours for p_0= 2 MPa

Close-Up View Near Detonation Front

This subsection discusses the effects of the high-resolution scheme near the rotating detonation front. Figures 5.11, 5.12, 5.13 and 5.14 show the instantaneous pressure, temperature, OH mass fraction, and local heat release contours near the rotating detonation front. Both schemes can capture some triple points near the rotating detonation front in the present grid resolution. Some disturbance in the temperature and OH mass fraction contours are captured behind the rotating detonation front for the WCNS5MN. The instantaneous profiles along i = 50∼300 are shown in Figs. 5.15, 5.16 and 5.17. The WCNS5MN can capture the large discontinuity near the detonation front better than the MUSCL as shown in Fig. 5.15. However, there are small difference on temperature and OH mass fraction in Figs. 5.16 and 5.17 because the WCNS5MN improves spatial resolution for fluid and this scheme does not improve resolution for chemical reaction as shown in Eqs. (5.25), (5.26) and (5.27).

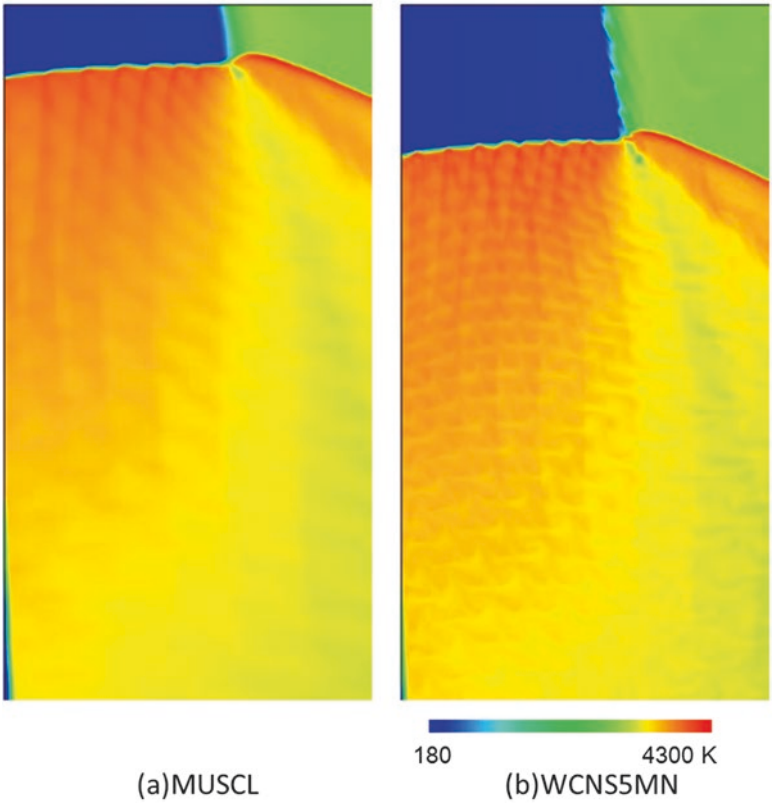

Fig. 5.12 Instantaneous temperature contours for p_0= 2 MPa

Detonation Velocity

Figure 5.18 shows the comparison of the rotating detonation velocity between the MUSCL and the WCNS5MN. The detonation velocity for both schemes is 2849 m/s and 97% of D_{CJ}. In the experimental data (Bykovskii et al. 2006), the rotating detonation velocities are 80–95% of D_{CJ} because of incomplete mixing and unconfined effects. The detonation velocity deficit in Hishida's 2D RDE simulation (Hishida et al. 2009) is approximately 5% because of the unconfined detonation effects. The present results agree well with those in Hishida's results (Hishida et al. 2009) .

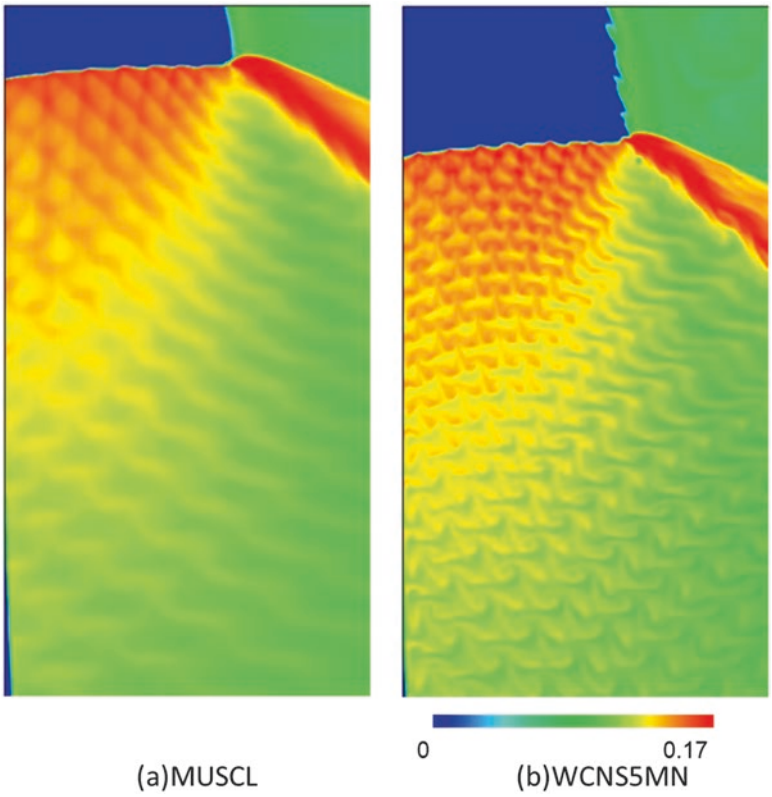

Fig. 5.13 Instantaneous OH mass fraction contours for p_0= 2 MPa

Thrust Performance

Figure 5.19 shows the comparison of I_{sp} between the MUSCL and the WCNS5MN. This figure also includes the calculated I_{sp} for a H_2/O_2 rocket engine without a diverging nozzle, assuming a chemical equilibrium state under a vacuum environment. This value is calculated using the Gordon and McBride method (Gordon and McBride 1971). This figure shows that I_{sp} for the WCNS5MN is approximately 5 sec larger than I_{sp} for the MUSCL. I_{sp} for both schemes is actually greater than I_{sp} of a conventional rocket engine.

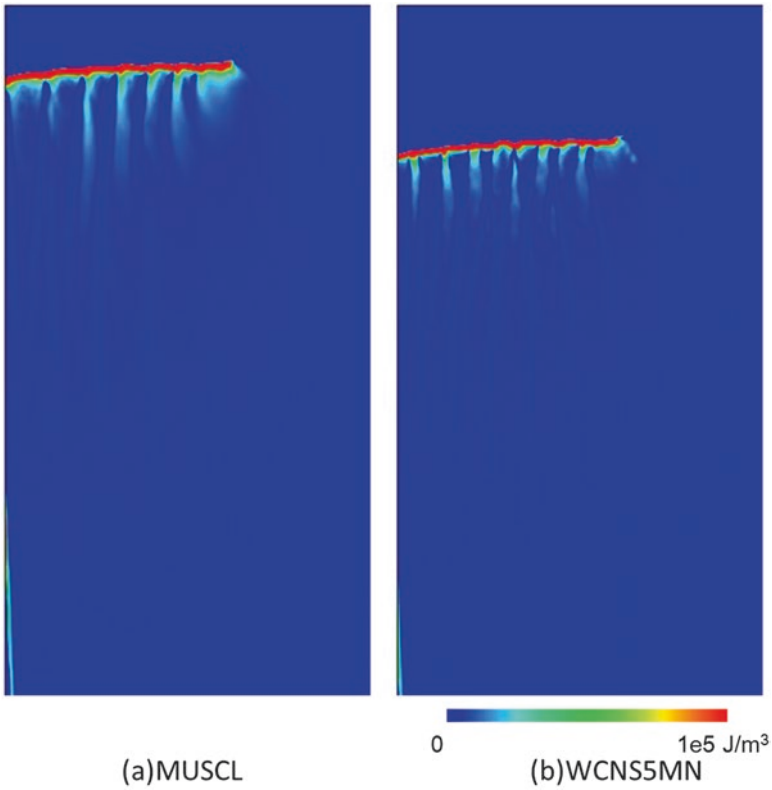

Fig. 5.14 Instantaneous heat release contours for p_0= 2 MPa

The time-averaged thrust per cycle for both schemes is also proportional to the mass flow rate, as shown in Fig. 5.20. Because the mass flow rates for the WCNS5MN are 2–4% smaller than those for the MUSCL, I_{sp} for the WCNS5MN is 5 s larger than I_{sp} for the MUSCL in Fig. 5.19.

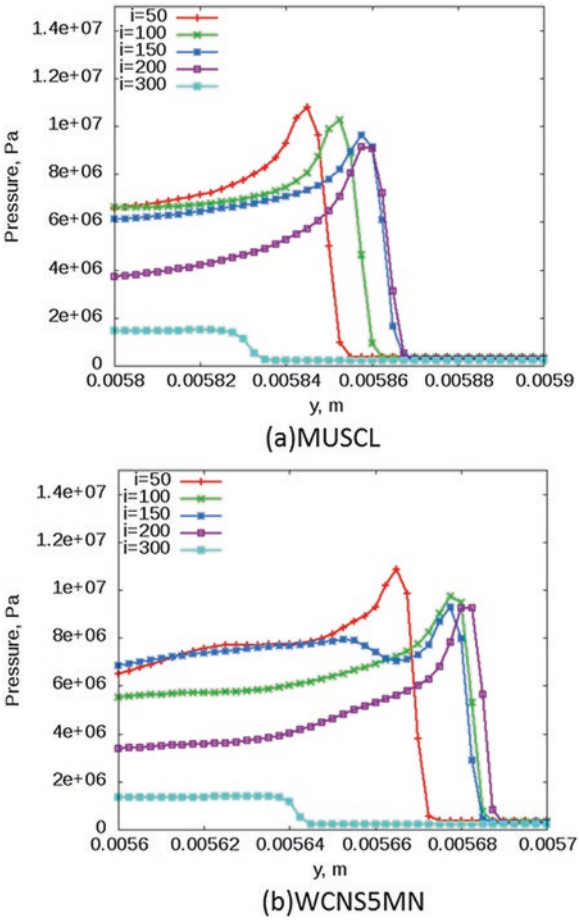

Fig. 5.15 Instantaneous pressure profiles near rotating detonation front along *y*-direction in Fig. 5.11 for p_0= 2 MPa

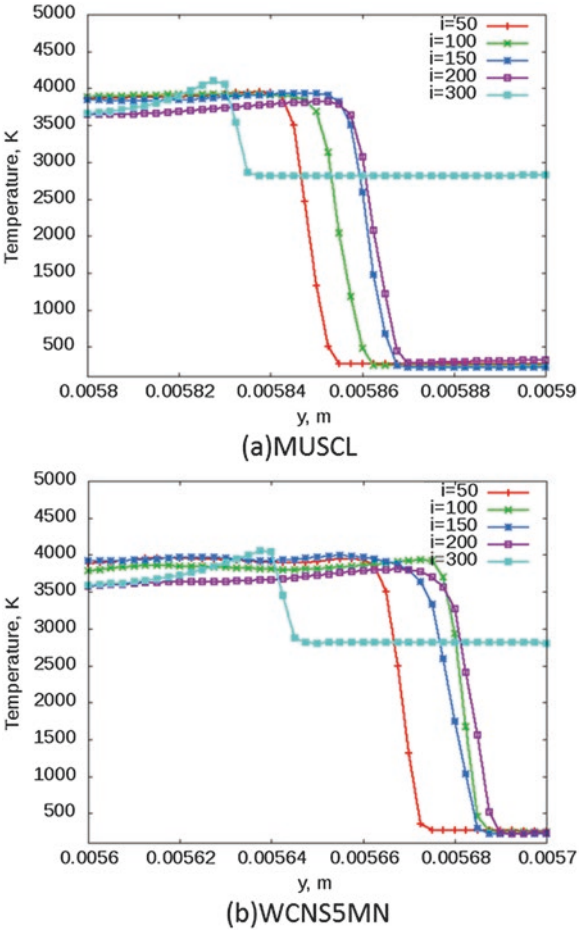

Fig. 5.16 Instantaneous temperature profiles near rotating detonation front along y-direction in Fig. 5.12 for p_0= 2 MPa

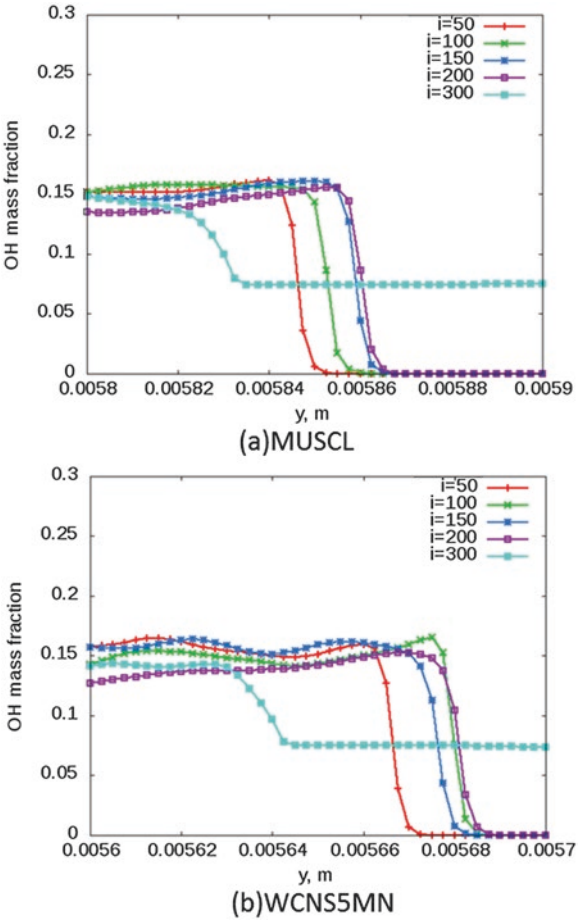

Fig. 5.17 Instantaneous OH mass fraction profiles near rotating detonation front along *y*-direction in Fig. 5.13 for p_0= 2 MPa

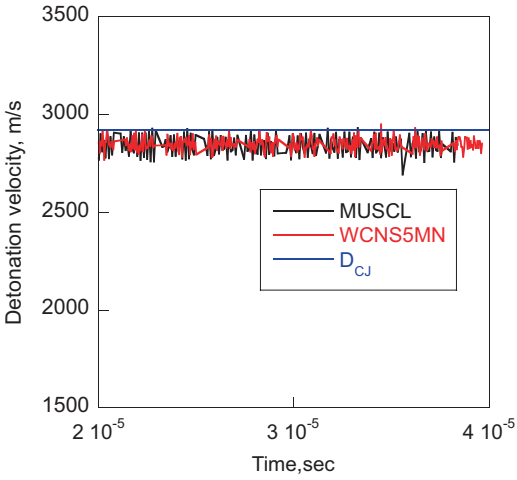

Fig. 5.18 Comparison of detonation velocities for p_0= 2 MPa

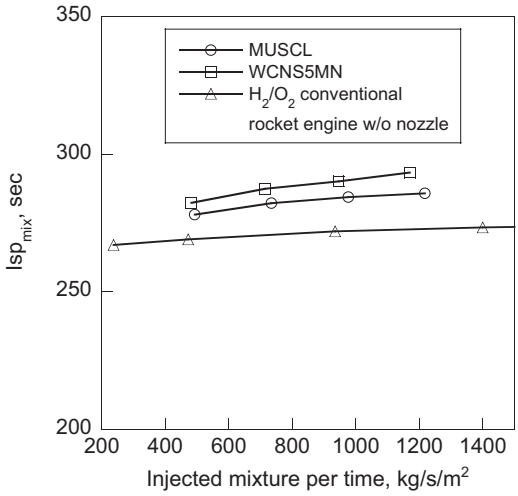

Fig. 5.19 Comparison of mixture-based specific impulse

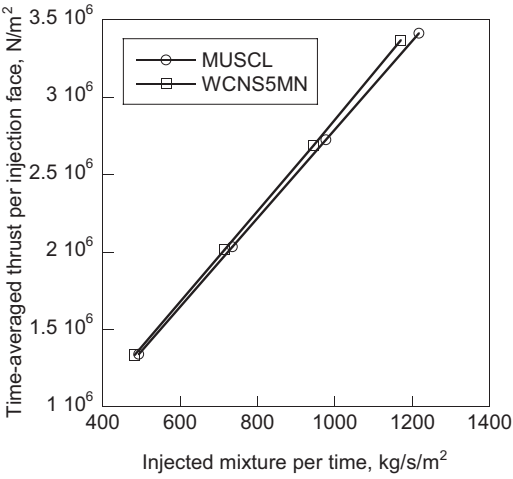

Fig. 5.20 Comparison of time-averaged thrust

7 Conclusions

The implementation and simulations of the robust weighted compact nonlinear scheme (RWCNS) for the two-dimensional rotating detonation engine are performed using the detailed chemistry model. The comparison of the MUSCL and the 5th-order RWCNS (WCNS5MN) indicates that the shock front and the contact surface for the WCNS5MN can be improved with the better resolution than those for the MUSCL and that both rotating velocities are approximately 97% of the CJ value. However, I_{sp} for the WCNS5MN is approximately 5 sec larger than I_{sp} for the MUSCL because the mass flow rates for the WCNS5MN are 2–4% smaller than those for the MUSCL.

Acknowledgements This research was done in collaboration with Cybermedia Center using the Osaka University supercomputer system.

References

Araki, T., Yoshida, K., Morii, Y., Tsuboi, N., & Hayashi, A. K. (2016). Numerical analyses on ethylene/oxygen detonation with multistep chemical reaction mechanisms: Grid resolution and chemical reaction model. *Combustion Science and Technology, 188*(3), 346–369.

Asahara, A., Hayashi, A. K., Yamada, E., & Tsuboi, N. (2012). Generation and dynamics of subtransverse wave of cylindrical detonation. *Combustion Science and Technology, 184*, 1568–1590.

Batten, P., Clarke, N., Lambert, C., & Causon, D. M. (1997). On the choice of wavespeeds for the HLLC Riemann solver. *SIAM Journal on Scientific Computing, 18*, 1553–1570.

Bykovskii, F. A., Zhdan, S. A., & Vedernikov, E. F. (2006). Continuous spin detonations. *Journal of Propulsion and Power, 22*(6), 1204–1216.

Davis, S. G., Joshi, A. V., Wang, H., & Egolfopoulos, F. (2005). An optimized kinetic model of H2/CO combustion. *Proceedings of the Combustion Institute, 30*(1), 1283–1292.

Deng, X. G., & Zhang, H. (2000). Developing high-order weighted compact nonlinear schemes. *Journal of Computational Physics, 165*, 22–44.

Einfeldt, B. (1988). On Godunov-type methods for gas dynamics. *SIAM Journal on Numerical Analysis, 25*, 294–318.

Eto, K., Tsuboi, N., & Hayashi, A. K. (2005). Numerical study on three-dimensional C-J detonation waves: Detailed propagating mechanism and existence of OH radical. *Proceedings of the Combustion Institute, 30*, 1907–1913.

Eto, S., Tsuboi, N., Takayuki, K., & Hayashi, A. K. (2016). Three-dimensional numerical simulation of a rotating detonation engine: Effects of the throat of a converging-diverging nozzle on engine performance. *Combustion Science and Technology, 188*(11–12), 2105–2116.

Godunov, S. K. (1959). A difference scheme for numerical solution of discontinuous solution of hydrodynamic equations. *Math. Sbornik, 43*, 271–306.

Gordon, S., & McBride, J.B. (1971). Computer program for calculation of complex chemical equilibrium compositions, rocket performance, incident and reflected shocks, and Chapman-Jouget detonations. NASA SP-273.

Gottlieb, S., & Shu, C. W. (1998). Total variation diminishing Runge-Kutta schemes. *Mathematics of Computation, 67*, 73–85.

Henrick, A. K., Aslam, T. D., & Powers, J. M. (2006). Simulations of pulsating one-dimensional detonations with true fifth order accuracy. *Journal of Computational Physics, 213*, 311–329.

Hishida, M., Fujiwara, T., & Wolanski, P. (2009). Fundamentals of rotating detonations. *Shock Waves, 19*(1), 1–10.

Hu, X. Y., Zhang, D. L., Khoo, B. C., & Jiang, Z. L. (2005). The structure and evolution of a twodimensional H2/O2/Ar cellular detonation. *Shock Waves, 14*, 37–44.

Iida, R., Asahara, M., Tsuboi, N., Hayashi, A. K., & Nonomura, T. (2014). Implementation of a robust weighted compact nonlinear scheme for modeling of hydrogen/air detonation. *Combustion Science and Technology, 186*(10–11), 1736–1757.

Jiang, G. S., & Shu, C. W. (1996). Efficient implementation of weighted ENO schemes. *Journal of Computational Physics, 126*, 200–212.

Konnov, A. A. (2008). Remaining uncertainties in the kinetic mechanism of hydrogen combustion. *Combustion and Flame, 152*(4), 507–528.

Korobenikov, V. P., Levin, V. A., Markov, V. V., & Chernyi, G. G. (1972). Propagation of blast wave in a combustible gas. *Astronautica Acta, 17*, 529–537.

Kurosaka, M., & Tsuboi, N. (2014). Spinning detonation, cross-currents, and the chapman-Jouguet velocity. *Journal of Fluid Mechanics, 756*, 728–757.

Li, J., Zhao, Z., Kazakov, A., & Dryer, F. L. (2004). An updated comprehensive kinetic model of hydrogen combustion. *International Journal of Chemical Kinetics, 36*(10), 566–575.

Mueller, M. A., Kim, T. J., Yetter, R. A., & Dryer, F. L. (1999). Flow reactor studies and kinetic modeling of the H2/O2 reaction. *International Journal of Chemical Kinetics, 31*(2), 113–125.

Niibo, T., Morii, Y., Ashahara, M., Tsuboi, N., & Hayashi, A. K. (2016). Numerical study on direct initiation of cylindrical detonation in H2/O2 mixtures: Effect of higher-order schemes on detonation propagation. *Combustion Science and Technology, 188*(11–12), 2044–2059.

Nonomura, T., & Fujii, K. (2009). Effects of difference scheme type in high-order weighted compact nonlinear schemes. *Journal of Computational Physics, 228*, 3533–3539.

Nonomura, T., & Fujii, K. (2013). Robust explicit formulation of weighted compact nonlinear scheme. *Computers and Fluids, 85*, 8–18.

Nonomura, T., Iizuka, N., & Fujii, K. (2010). Freestream and vortex preservation properties of highorder WENO and WCNS on curvilinear grids. *Computers and Fluids, 39*, 197–214.

Nonomura, T., Morizawa, S., Terashima, H., Obayashi, S., & Fujii, K. (2012). Numerical (error) issues on compressible multicomponent flows using a high-order differencing scheme: Weighted compact nonlinear scheme. *Journal of Computational Physics, 231*, 3181–3210.

O'Conaire, M. O., Curran, H. J., Simmie, J. M., Pitz, W. J., & Westbrook, C. K. (2004). A comprehensive modeling study of hydrogen oxidation. *International Journal of Chemical Kinetics, 36*(11), 603–622.

Odlyzko, A. M. (1985). Discrete logarithms in finite fields and their cryptographic significance. *Lecture Notes in Computer Science, 209*, 224–314.

Oran, E. S., Young, T., & Boris, J. P. (1979). Application of time-dependent numerical methods to the description of reactive shocks. *Seventeenth Symposium (International) on Combustion*, 43–54.

Petersen, E. L., & Hanson, R. K. (1999). Reduced kinetics mechanisms for ram accelerator combustion. *J. Propulsion Power, 15*, 591–600.

Saxena, P., & Williams, F. A. (2006). Testing a small detailed chemical-kinetic mechanism for the combustion of hydrogen and carbon monoxide. *Combustion and Flame, 145*(1–2), 316–323.

Schwer, D., & Kailasanath, K. (2013). Fluid dynamics of rotating detonation engines with hydrogen and hydrocarbon fuels. *Proceedings of the Combustion Institute, 34*, 1991–1998.

Shepherd, J. E. (1986). Chemical kinetics of H2-air-diluent detonations. In*Progr. in Astronautics and aeronautics* (Vol. 106, pp. 263–293).

Shimizu, K., Hibi, H., Koshi, M., Morii, M., & Tsuboi, N. (2011). Updated kinetic mechanism for high-pressure hydrogen combustion. *Journal of Propulsion and Power, 27*(2), 383–396.

Shuen, J. S. (1992). Upwind differencing and LU factorization for chemical non-equilibrium Navier-stokes equations. *Journal of Computational Physics, 909*, 233–250.

Stull, D. R., & Prophet, H. (1971). *JANAF Thermochemical Tables* (2nd ed.). NSRDS-NBS, 37.

Togashi, F., Lohner, R., & Tsuboi, N. (2009). Numerical simulation of H2/air detonation using unstructured mesh. *Shock Waves, 19*(2), 151–162.

Tsuboi, N., & Koichi Hayashi, A. (2007). Numerical study on spinning detonations. *Proceedings of the Combustion Institute, 31*, 2389–2396.

Tsuboi, N., Katoh, S., & Hayashi, A. K. (2002). Three-dimensional numerical simulation for hydrogen/air detonation: Rectangular and diagonal structures. *Proceedings of the Combustion Institute, 29*, 2783–2788.

Tsuboi, N., Eto, K., & Hayashi, A. K. (2007). Detailed structure of spinning detonation in a circular tube. *Combustion and Flame, 149*(1–2), 144–161.

Tsuboi, N., Asahara, M., Eto, K., & Hayashi, A. K. (2008a). Numerical simulation of spinning detonation in square tube. *Shock Waves, 18*(4), 329–344.

Tsuboi, N., Daimon, Y., & Hayashi, A. K. (2008b). Three-dimensional numerical simulation of detonations in coaxial tubes. *Shock Waves, 18*(5), 379–392.

Tsuboi, N., Hayashi, A. K., & Koshi, M. (2009). Energy release effect of mixture on single spinning detonation structure. *Proceedings of the Combustion Institute, 32*, 2405–2412.

Tsuboi, N., Morii, Y., & Koichi Hayashi, A. (2013). Two-dimensional numerical simulation on galloping detonation in a narrow channel. *Proceedings of the Combustion Institute, 34*(2), 1999–2007.

Tsuboi, N., Eto, S., Hayashi, A. K., & Kojima, T. (2017). Front cellular structure and thrust performance on hydrogen-oxygen rotating detonation engine. *Journal of Propulsion and Power, 33*(1), 100–111.

Tsuboi, N., Watanabe, Y., Kojima, T., & Hayashi, A. K. (2015). Numerical estimation of the thrust performance on a rotating detonation engine for a hydrogen-oxygen mixture. *Proceedings of the Combustion Institute, 35*(2), 2005–2013.

Wada, Y., & Liou, M. (1994). A flux splitting scheme with high resolution and robustness for discontinuities. *AIAA Paper, 94-0083*, 1994.

Wintenberger, E., & Shepherd, J. E. (2003). A model for the performance of air-breathing pulse detonation engines. *AIAA Paper, 03-4511*, 2003.

Yee, H. C. (1987). Upwind and symmetric shock-capturing schemes. NASA TM-89464.

Zhang, S., Jiang, S., & Shu, C. W. (2008). Development of nonlinear weighted compact schemes with increasingly higher order accuracy. *Journal of Computational Physics, 227*, 7294–7321.

Zhdan, S. A., Bykovskii, F. A., & Vedernikov, E. F. (2007). Mathematical modeling of a rotating detonation wave in a hydrogen-oxygen mixture. *Combustion, Explosion and Shock Waves, 43*(4), 449–459.

Zhou, R., & Wang, J. P. (2012). Numerical investigation of flow particle paths and thermodynamic performance of continuously rotating detonation engines. *Combustion and Flame, 159*, 3632–3645.